Proton elastic scattering at 200 A MeV and high momentum transfers of 1.7–2.7 fm^{-1} as a probe of the nuclear matter density of ^{6}He

S. Chebotaryov[1,2], S. Sakaguchi[1,3,*], T. Uesaka[1], T. Akieda[4], Y. Ando[2], M. Assie[5], D. Beaumel[5], N. Chiga[1], M. Dozono[6], A. Galindo-Uribarri[7], B. Heffron[7], A. Hirayama[8], T. Isobe[1], K. Kaki[9], S. Kawase[10], W. Kim[2], T. Kobayashi[4], H. Kon[4], Y. Kondo[8], Y. Kubota[1], S. Leblond[11], H. Lee[11], T. Lokotko[11], Y. Maeda[12], Y. Matsuda[13], K. Miki[4], E. Milman[1,2], T. Motobayashi[1], T. Mukai[4], S. Nakai[4], T. Nakamura[8], A. Ni[2], T. Noro[3], S. Ota[6], H. Otsu[1], T. Ozaki[8], V. Panin[1], S. Park[2], A. Saito[8], H. Sakai[1], M. Sasano[1], H. Sato[1], K. Sekiguchi[4], Y. Shimizu[1], I. Stefan[5], L. Stuhl[1], M. Takaki[6], K. Taniue[12], K. Tateishi[1], S. Terashima[14], Y. Togano[8], T. Tomai[8], Y. Wada[4], T. Wakasa[3], T. Wakui[15], A. Watanabe[4], H. Yamada[8], Zh. Yang[1], M. Yasuda[8], J. Yasuda[3], K. Yoneda[1], and J. Zenihiro[1]

[1]*RIKEN Nishina Center for Accelerator-Based Science, RIKEN, Saitama 351-0198, Japan*
[2]*Department of Physics, Kyungpook National University, Daegu 41566, Republic of Korea*
[3]*Department of Physics, Kyushu University, Fukuoka 819-0395, Japan*
[4]*Department of Physics, Tohoku University, Miyagi 980-8578, Japan*
[5]*Institut de Physique Nucléaire, Orsay 91406, France*
[6]*Center for Nuclear Study, University of Tokyo, Tokyo 113-0033, Japan*
[7]*Oak Ridge National Laboratory, Oak Ridge, TN 37830, USA*
[8]*Department of Physics, Tokyo Institute of Technology, Tokyo 152-8551, Japan*
[9]*Department of Physics, Shizuoka University, Shizuoka 422-8529, Japan*
[10]*Department of Advanced Energy Engineering Science, Kyushu University, Fukuoka 816-8580, Japan*
[11]*Department of Physics, University of Hong Kong, Pokfulam Road 999077, Hong Kong*
[12]*Department of Applied Physics, University of Miyazaki, Miyazaki 889-2192, Japan*
[13]*Cyclotron and Radioisotope Center, Tohoku University, Miyagi 980-8578, Japan*
[14]*Department of Physics, Beihang University, Beijing 100191, China*
[15]*National Institute of Radiological Sciences, Chiba 263-8555, Japan*
*E-mail: sakaguchi@phys.kyushu-u.ac.jp

....

Differential cross sections of p–^{6}He elastic scattering were measured in inverse kinematics at an incident energy of 200 A MeV, covering the high momentum transfer region of 1.7–2.7 fm^{-1}. The sensitivity of the elastic scattering at low and high momentum transfers to the density distribution was investigated quantitatively using relativistic impulse approximation calculations. In the high momentum transfer region, where the present data were taken, the differential cross section has an order of magnitude higher sensitivity to the inner part of the ^{6}He density relative to the peripheral part (15:1). This feature makes the obtained data valuable for the deduction of the inner part of the ^{6}He density. The data were compared to a set of calculations assuming different proton and neutron density profiles of ^{6}He. The data are well reproduced by the calculation assuming almost the same profiles of proton and neutron densities around the center of ^{6}He, and a proton profile reproducing the known point-proton radius of 1.94 fm. This finding is consistent with the assumption that the ^{6}He nucleus consists of a rigid α-like core with a two-neutron halo.
....

Subject Index   D11, D27

1. Introduction

The study of the structure and reactions of nuclei away from the stability line is at the forefront of research in modern nuclear physics. Due to the large difference between neutron and proton numbers in unstable nuclei, they are known to occasionally reveal a qualitatively new phase of nuclear structure. Observed in drip line nuclei, one of the most prominent examples is the so-called neutron halo. The main characteristic of the halo is a long tail in the density distribution of the nucleus. It is a direct consequence of the extremely low separation energies of valence neutrons in drip line nuclei ($E_s < 1$ MeV) compared to the stable ones ($E_s = 6$–8 MeV). Halos are formed primarily by s- and p-state wave functions, as such states have no or low orbital angular momentum. Tunneling of the halo wave function into the classically forbidden region of a strong force range forms a low-density tail component, which violates the saturation property of the nuclear matter. This presents new possibilities to study interesting features of low-density neutron matter, such as spatial or momentum correlations of neutrons constituting the halo. Nuclei with two neutron halos are of special interest, as, in most cases, their binary subsystems are unbound. Such nuclei, which exist only in three-body bound states, are called Borromean. It is of real interest to understand why a three-body system is still bound. Due to their distinctive features, halo nuclei naturally become an attractive target for experimental studies. Knowledge on spatial structures would be a key to a better understanding of various aspects of such nuclei.

One of the most fundamental ways to experimentally study the spatial structure of a nucleus is to probe its radial density distributions. Several experimental approaches exist for this. Historically, one of the first and most reliable ways to extract information on the charge distribution of stable nuclei is via electron elastic scattering [1], as the interaction is purely electromagnetic and hence is well known. Proton elastic scattering has been successfully applied to probe the density distributions of both stable and unstable nuclei [2–12], and is regarded as one of the most reliable ways to extract neutron and total matter densities. The combined information from electron and proton scattering allows the separate determination of proton and neutron distributions of stable nuclei. Knowledge of both proton and neutron densities is especially important in the case of unstable neutron- or proton-rich nuclei, where, e.g., neutron skins and halos emerge. Due to the lack of electron scattering data for unstable nuclei, the extraction of proton and neutron densities is difficult. A new scheme that was recently implemented at SCRIT [13] makes it possible to study the charge distribution of unstable nuclei via electron scattering.

The present work aims to extract new information on the density distribution of ^{6}He via proton elastic scattering at high momentum transfer. Neutron-rich ^{6}He is a prime example of a halo nucleus. It is the lightest known Borromean halo. Owing to its small number of nucleons, it is the easiest system to treat from a theoretical standpoint. Due to its features, ^{6}He has been extensively studied, both experimentally and theoretically. From the measurement of the interaction cross section, firsthand information on its matter radius was obtained [14]. Proton elastic scattering was used to confirm the presence of the halo and to study its radial matter distribution [4–7,9]. Recently, its charge radius was precisely determined from laser spectroscopy measurements [15]. The obtained value for the charge radius is 2.054 ± 0.014 fm, with a corresponding point-proton radius of 1.912 ± 0.018 fm.

So far, the measurements of the differential cross sections of p–^{6}He elastic scattering have been limited to the relatively low momentum transfer region of $q < 2.0$ fm^{-1}. It is shown in several existing works that sensitivity to the details of the density distribution depends on the momentum transfer region [4,16,17]. To reveal the details of the density distribution in the interior of a nucleus,

high momentum transfer data are necessary [16]. Knowledge on the interior region is important as well to tag the existence of the halo. Since the nuclear densities in the interior and exterior regions both contribute to the differential cross sections, it is not easy to determine the density of the halo part without precise knowledge of the core part. Current knowledge on the density distribution of ^{6}He was obtained mostly from the data measured at low momentum transfers [4–7]. While such data are sufficient to probe the extension of nuclear matter in the nuclear exterior region, they might not suffice to probe the shape of the density distribution beyond the nuclear surface. A recent study [17] using elastic scattering data in a wide momentum transfer region of $q = 0.2$–2.0 fm^{-1} confirmed that high momentum transfer data are important to deduce the density distribution with high accuracy, especially for the nuclear interior. Such data are a valuable source of information on the details of the nuclear density distribution. We consider it to be important to obtain new experimental data taken at higher momentum transfers, as it allows the deduction of the density distribution in the core region of ^{6}He with high accuracy.

In our experiment, the p–^{6}He cross sections were measured at an incident energy of 200 A MeV. These are the first data to cover high momentum transfers up to 2.7 fm^{-1} ($q = 1.7$–2.7 fm^{-1}), and are a new source of information on the density of the ^{6}He nucleus, especially its core part. Our data can complement the existing measurements carried out at a lower momentum transfer [7,9], and are expected to be sensitive to the density of ^{6}He in a wider region. Thus, the overall shape of the density distribution can be deduced with high accuracy. An incident energy of 200 A MeV was chosen, as the probe particle has a long mean free path at this energy, and single-collision scattering will be the dominant process. Also, in this energy region, there exist several theoretical predictions of p–^{6}He elastic scattering, which are based on different reaction models [18–20].

In Sect. 2, the experiment and the data analysis procedure are described. In Sect. 3 the obtained experimental results are presented. Section 4 describes the theoretical analysis of the obtained data.

2.   Experiment and data analysis

2.1.   Experiment

This experiment was performed at the RI Beam Factory (RIBF) [21] operated by RIKEN Nishina Center and CNS, University of Tokyo. A secondary beam of unstable ^{6}He particles was produced via a fragmentation reaction of a 230 A MeV ^{18}O primary beam on a 15 mm thick Be target (2.8 g/cm^2) [22] installed at the F0 focal plane of BigRIPS (Big RI Projectile Separator) [23]. After the fragmentation, the secondary beam species went through the first stage of BigRIPS, where the fragments were separated according to their momentum and A/Z ratio. Special care was taken to reduce beam contamination by tritons as their production rate was anticipated to be much higher relative to ^{6}He. It was suppressed with a collimator and momentum selection slit at the F2 achromatic focal plane. A collimator made of iron with a thickness of 300 mm and horizontal and vertical openings of 24×44 mm^2 was used. The opening widths of the slit were set to 2×2 mm^2. After separation, the beam was transported to the F13 focal plane, which is located at the secondary target position, upstream of the SAMURAI magnetic spectrometer [24], where the observed triton contamination was as small as 6%. To reduce the size of the beam spot at the secondary target, we minimized the distance between the last quadrupole magnet (STQ25) and the secondary target. The experimental setup at F13 is schematically shown in Fig. 1. The distance between the downstream edge of the magnet and the secondary target was 2.6 m. A ^{6}He beam with a purity of 94% was obtained at F13, with incident energies of 200 ± 2 A MeV and an intensity of 1×10^6 pps at the maximum. For the safe operation of the beamline drift chambers, the beam intensity was kept at
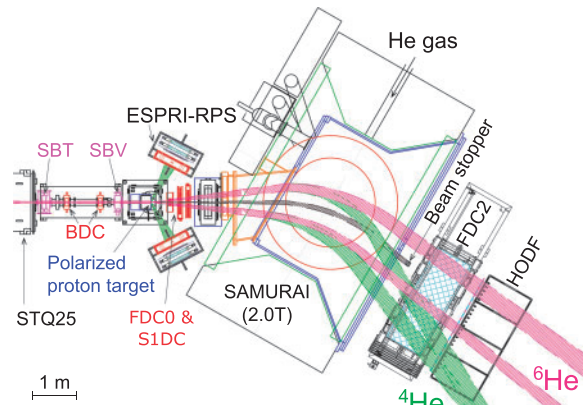
Fig. 1. Top view of the experimental setup at the SAMURAI site.

6×10^5 pps. A beam profile with a Gaussian-like shape and 5 mm widths in sigma was achieved at the target.

Downstream of the STQ25, two 2 mm thick plastic scintillators (SBTs) were installed for the detection of beam particles, as shown in Fig. 1. The SBTs were used to produce the beam trigger and to carry out particle identification by energy loss measurement (ΔE). The beam trigger threshold was set for particles with an atomic number of $Z \geq 2$. Downstream from the SBTs, two multi-wire drift chambers (MWDCs) were installed (BDC1/2) [25] for tracking of the beam particles. The combined tracking efficiency of the two BDCs was 97%, which remained almost constant even at high beam rates of up to 1×10^6 pps. The tracking efficiencies of all MWDCs used in the present experiment were obtained by evaluating the single-wire efficiency of each MWDC layer. The position resolution on the secondary target was 0.4 mm in sigma. A veto scintillator (SBV) was used to suppress beam trigger generation by the particles from the beam halo hitting thick materials around the target. The SBV is a plastic scintillator with a 10 mm thick plate having a $\phi 18$ mm hole in the center, which was designed to be slightly smaller than the target size of $\phi 24$ mm. It was installed at a distance of 730 mm upstream of the target.

A solid spin-polarized proton target was installed downstream of the SBV [26]. The aim of the experiment was not only to measure the differential cross sections, but also to obtain the analyzing power, which will be the subject of future publications. The material of the polarized target is a single crystal of naphthalene ($C_{10}H_8$), which was chosen for its polarizability features. The crystal was shaped as a disk, 24 mm in diameter and 2.5 mm in thickness (285 mg/cm^2).

For the detection of recoil particles, we used a pair of recoil proton spectrometers (RPSs) placed at both the left and right sides of the beamline. The spectrometers were developed for the Elastic Scattering of Protons by RI beams project (ESPRI) at RIKEN [27]. Each detector consists of an MWDC for recoil-particle tracking (recoil drift chamber (RDC)), a 4 mm thick plastic scintillator (BC-408) for energy loss measurement, and an array of seven NaI(Tl) scintillators for total energy measurement. The NaI(Tl) scintillators cover proton energies up to 100 MeV, while, in our experiment, energies of recoil protons were up to 160 MeV. To limit the maximum energy of recoil protons incident on NaI(Tl) at forward angles, a wedge-shaped energy degrader was installed in between the RDC and the plastic scintillator, as shown in Fig. 2. The degrader was made of brass and had a width of 230 mm and a thickness in the range of 4–30 mm; it could degrade the proton energy from 100–160 MeV to below 100 MeV. The angular straggling due to the degrader was less than 55 mrad
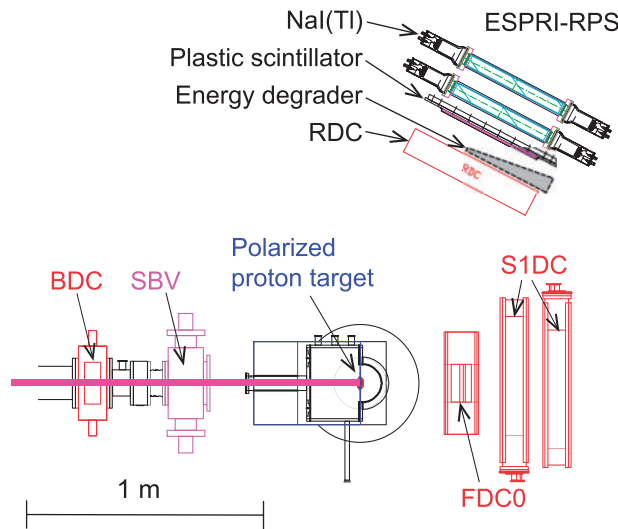
Fig. 2. Experimental setup around the target system.

in sigma, and did not severely affect the acceptance of NaI(Tl). The energy spread caused by multiple scattering in the degrader material was less than 2% of the proton energy after it passed through the degrader, and did not affect the condition of the event selection. The attenuation of the proton flux due to the reaction loss in the degrader material was compensated in the data analysis. For this, the proton flux attenuation was calculated as a function of the recoil proton angle using the value of the proton reaction cross section from Ref. [28]. The thickness of the energy degrader material as a function of recoil proton angle was computed using the degrader geometry. The attenuation reached 13% at the thickest part of the degrader covered by the acceptance of the detection setup (25 mm thick). Spectrometers were placed at a distance of 1 m away from the target. The RPS system covered an angular region of 55–70 deg in the laboratory frame. The tracking efficiency of the RDCs was deduced to be 72%, which is a relatively low value possibly due to a high-noise condition or a hidden gas leak. There was no noticeable dependence of the tracking efficiency on the position or energy of the incident particle.

In order to track the scattered particles, two drift chambers, namely FDC0 and S1DC, were installed downstream of the target at distances of 400 and 737 mm, respectively (see Fig. 2 for details). FDC0 has an effective area of 160×160 mm^2 and a wire spacing of 5 mm. S1DC has an effective area of 480×240 mm^2 and a wire spacing of 12 mm. The tracking efficiencies were 99.8% and 89% for FDC0 and S1DC, respectively. FDC0 was used for the p–^{6}He measurement, taking advantage of its high-rate tolerance, and S1DC was used for the p–^{4}He calibration measurement, taking advantage of its large angular coverage.

The scattered particles entered into the SAMURAI magnetic spectrometer [25] after passing through FDC0 and S1DC. SAMURAI was used to discriminate ^{6}He breakup channels by carrying out A/Z analysis of the scattered particles. A vacuum chamber in the spectrometer gap was filled with helium gas at 1 atm. This was done to reduce the material thickness compared to air, since it was not possible to evacuate the chamber on which a 5.2 m wide large exit window was attached to maximize its acceptance. The air in the chamber was replaced by the flow of helium gas for about 24 h. After the replacement, the concentration of helium gas in the chamber reached 95% and stayed constant during the experiment. On the downstream side of SAMURAI, a drift chamber (FDC2) [25] and a wall of 24 plastic scintillators (HODF) [25] were installed for the measurement
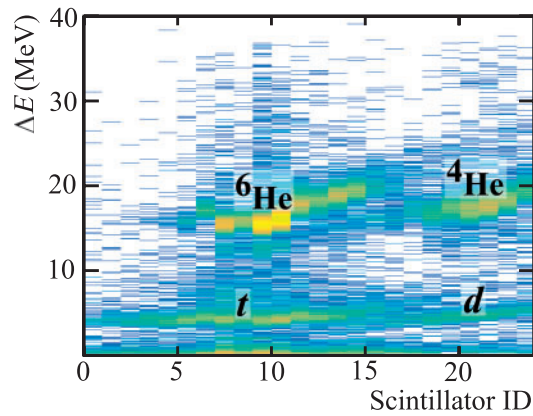
Fig. 3. Energy loss spectra of incoming particles at the HODF plastic scintillators.

of trajectory and energy loss of the scattered particles. A beam stopper, which was a lead block with dimensions of $10 \times 10 \times 40$ cm, was installed just in front of FDC2 to prevent it from being damaged by the intense unreacted beam. The background events resulting from the unreacted beam hitting the beam stopper were excluded using information on the ^{6}He scattering angle from the drift chambers installed upstream of the SAMURAI spectrometer (FDC0 and S1DC).

The main trigger was produced by the coincidence detection of the beam, using the signal from the SBT detector, and a recoil particle, using the signal from the ESPRI-RPSs plastic scintillator. The typical trigger rate was $\sim 5 \times 10^2$ cps. The p–^{6}He elastic scattering measurement was carried out for 3 days. Data of p–^{4}He elastic scattering were taken to check the performance of the detection setup and validity of the analysis procedure by reproducing the existing data obtained by Moss et al. [29]. After p–^{6}He measurements, the beam was switched to ^{4}He, and p–^{4}He elastic scattering was measured for 1 day. The background data using a pure carbon target were also taken, in order to subtract the contribution from carbon nuclei contained in the polarized target material. The size of the carbon target was 24 mm in diameter and 1.2 mm in thickness (220 mg/cm^2). This measurement was carried out with the ^{6}He beam for 1 day.

2.2. Data analysis

p–^{6}He elastic scattering can be identified as a coincident detection of scattered ^{6}He and a recoil proton, since ^{6}He has no bound excited state. The major contaminant events resulted from the breakup of ^{6}He due to its low binding nature. The yield of such events far exceeded that of elastic scattering. The breakup channel can be removed by identifying the scattered particles. Another contribution is from the quasi-free scattering (QFS) of ^{6}He on protons in the carbon contained in the target material. The materials in the target chamber did not contain free hydrogens in their chemical composition, thus eliminating secondary sources of elastic scattering events. The procedure of data reduction is described below.

Forward-focused scattered particles were identified through A/Z analysis using the SAMURAI spectrometer. The energy loss spectrum of the particles hitting the HODF is shown in Fig. 3. The horizontal axis shows the plastic scintillator ID of the HODF detector, where an ID of 0 corresponds to the highest momentum side, while an ID of 23 corresponds to the lowest momentum side; the vertical axis shows the energy loss (ΔE) of a scattered particle. Clear loci of ^{6}He and ^{4}He along with triton and deuteron contaminants resulting from the breakup of ^{6}He can be seen. The identification of loci was done by performing a Monte Carlo simulation of the energy loss spectra of the particles
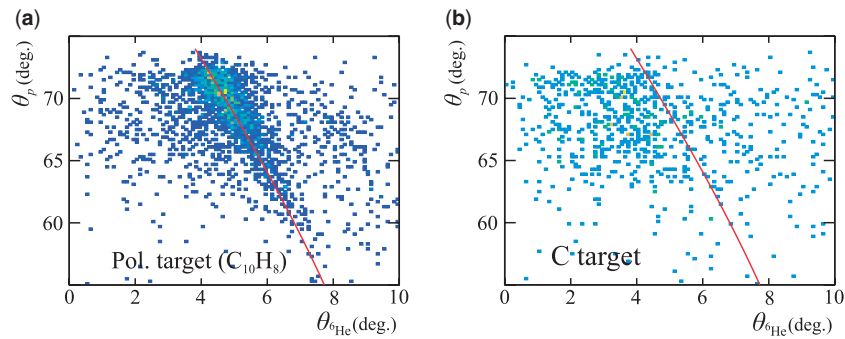
Fig. 4. Correlation of polar angles of scattered/recoil particles. The horizontal axes show ^{6}He angles, while the vertical axes show proton angles. The figure shows the data from polarized (a) and carbon (b) targets.

at the HODF detector before the experiment. The breakup of ^{6}He in the target material was easily discriminated by the SAMURAI spectrometer as the energy per nucleon of the scattered ^{6}He and the broken-up ^{4}He fragment is almost the same, while their mass is 1.5 times different. Due to the big mass difference, momentum analysis of events when ^{6}He breaks up in the target was done very reliably. It is also possible that ^{6}He breaks up after the momentum analysis, e.g., when a ^{6}He particle hits one of the HODF plastic scintillators. In this case the energy deposit can become slightly lower than that of ^{6}He, and a low-energy tail can be observed in Fig. 3, right below the main locus of ^{6}He events. The gate width of ΔE was set wide enough to include such events. After discrimination of the breakup channel, only elastic scattering and QFS events are left. The QFS events resulted from beam particles hitting materials located close to the beamline, such as devices inside the target chamber, and those on the beamline, such as the carbon contained in the target material. The former were removed by rejecting the events in which the beam particle position on the target was at a distance of 9 mm or further from the target center. To remove the latter, kinematical information from the elastic scattering was used. Figure 4(a) shows the correlation of the polar angles of the scattered (horizontal axis) and recoil (vertical axis) particles from the polarized target data, while Fig. 4(b) shows the same for the carbon target. The red curves show the correlation of polar angles corresponding to p–^{6}He elastic scattering. The locus of the elastic scattering can be easily identified in Fig. 4(a). Figure 4(b) shows a locus corresponding to QFS events from carbon, which partly overlaps with the locus of elastic scattering. The subtracted contribution from the carbon target was an order of magnitude lower than the true events. Figure 5 shows the distribution of QFS event yields (dotted line) as a function of the recoil proton polar angle compared with that of polarized target yields (solid line). The resulting proton spectrum after subtraction of QFS events gave a high signal-to-noise ratio for the selection of elastic scattering events. Lastly, a cut on the polar angle of ^{6}He was defined to be ± 1.5 deg from the elastic scattering kinematics, shown by the solid red line. This was done to ensure that only events that are well correlated with elastic scattering kinematics are selected and to improve the signal-to-noise ratio further.

The deduction of p–^{4}He cross sections was carried out in a way similar to that of p–^{6}He, with an aim to confirm the adequacy of the data analysis procedure. The only difference in analysis was the method used to subtract QFS events. To do this, instead of taking the carbon target data with the ^{4}He beam, a coplanarity condition was used. In the case of elastic scattering, the difference in azimuthal angles of a proton and a scattered particle is 180 deg, since the final state is a binary system. However, the azimuthal angle difference has more spread in the case of other channels, since their final states
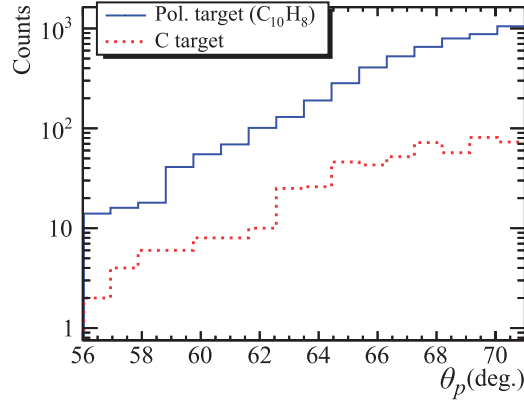
Fig. 5. Yields from the polarized (solid line) and carbon (dotted line) targets as a function of the recoil proton polar angle. The horizontal axis shows the laboratory angle of the recoil proton, and the vertical axis shows yields.
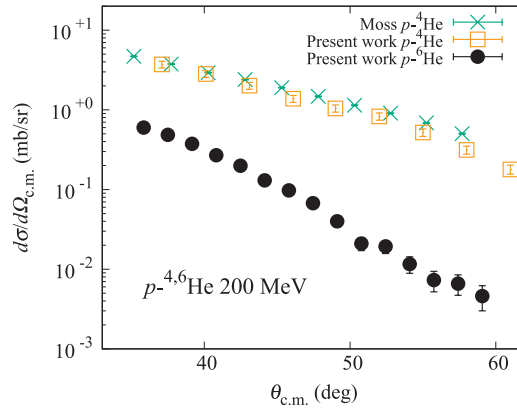

Fig. 6. Differential cross sections of p–^{4}He elastic scattering measured in the present work (open squares) and previous data (crosses) obtained by Moss et al. [29]. The experimental result of the p–^{6}He elastic scattering cross sections measured in the present work is shown by filled circles.

consist of more than two particles. Apart from this, the analysis of p–^{4}He data was done in essentially the same way as that for p–^{6}He.

The absolute values of p–^{4,6}He differential cross sections were deduced by using the obtained yields and the number of beam and target nuclei. To avoid event loss in the obtained yields due to possible differences in the acceptances of the detectors used, the acceptance region of the whole detection setup was defined so that the same overlapping region is covered by each detector. The obtained yields were normalized using the deduced efficiency values of all MWDCs. By checking single-wire efficiencies, the position-dependent deviation of the tracking efficiency from its mean value for the RDCs FDC0 and S1DC was found to be less than 5%.

3.   Experimental results

Figure 6 shows differential cross sections of p–^{4}He and p–^{6}He elastic scattering at 200 A MeV obtained in this experiment. The main purpose of measuring p–^{4}He cross sections is to compare them to the existing data obtained by Moss et al. [29], which are also given in Fig. 6. This was done to confirm the validity of the measurement and the data analysis procedure. A good agreement was obtained between the present and existing p–^{4}He data without performing any arbitrary

Table 1. Differential cross sections of p–^{6}He elastic scattering at 200 A MeV. The error $\Delta(d\sigma/d\Omega_{\mathrm{c.m.}})$ is defined as a root sum square of the statistical and systematic uncertainties, where the systematic uncertainty is 9.4%.

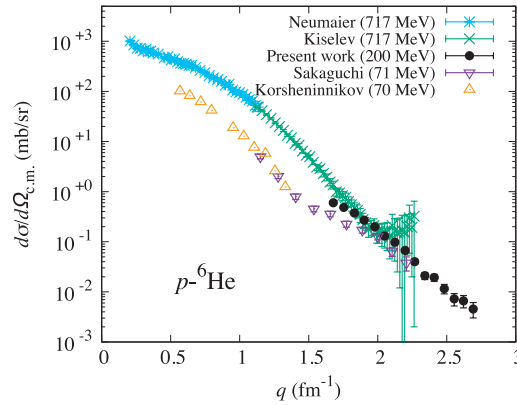| $\theta_{\mathrm{c.m.}}$ (deg)	$\frac{d\sigma}{d\Omega_{\mathrm{c.m.}}}$ (mb/sr)	$\Delta(\frac{d\sigma}{d\Omega_{\mathrm{c.m.}}})$ (mb/sr)
35.8	6.00×10^{-1}	5.99×10^{-2}
37.5	4.86×10^{-1}	4.89×10^{-2}
39.2	3.74×10^{-1}	3.82×10^{-2}
40.8	2.70×10^{-1}	2.81×10^{-2}
42.5	1.99×10^{-1}	2.13×10^{-2}
44.1	1.30×10^{-1}	1.47×10^{-2}
45.8	9.75×10^{-2}	1.15×10^{-2}
47.5	6.73×10^{-2}	8.06×10^{-3}
49.1	3.99×10^{-2}	5.85×10^{-3}
50.8	2.10×10^{-2}	3.92×10^{-3}
52.4	1.93×10^{-2}	3.61×10^{-3}
54.1	1.16×10^{-2}	2.71×10^{-3}
55.8	7.26×10^{-3}	2.13×10^{-3}
57.4	6.60×10^{-3}	1.92×10^{-3}
59.1	4.56×10^{-3}	1.60×10^{-3}

Fig. 7. Summary of the measured differential cross sections of p–^{6}He elastic scattering. The figure shows data from the present experiment (filled circles), and data from previous experiments [4,11,30,31].

normalization. The numerical data of the obtained p–^{6}He cross sections with total errors are given in Table 1. Absolute values of the differential cross sections in the center-of-mass (c.m.) frame in Table 1 correspond to bin-averaged values in the laboratory frame, where the angular width of a bin was 0.9 deg. The values of the center-of-mass angle correspond to the bin centers. The total error $\Delta(d\sigma/d\Omega_{\mathrm{c.m.}})$ is defined as the root sum square of statistical and systematic errors. The systematic error in our measurement was determined to be 9.4%. The main contribution to the systematic error (7.7%) resulted from the event selection procedure, where the robustness was checked by varying the angular cut width. Other noticeable contributions originated from the uncertainties in the tracking efficiencies of MWDCs (5.0%) and the uncertainty in determination of the target thickness (1.9%).

Figure 7 shows the p–^{6}He differential cross sections at 200 A MeV, obtained in the present experiment, along with the results of previous experiments for comparing the momentum transfer regions that were measured. Data from the present work were obtained in the highest momentum transfer

region $q = 1.7$–2.7 fm^{-1} with relatively small uncertainties in comparison to the previous measurements. At backward angles, they cover up to the second diffractive minimum. A good sensitivity to the details of the density distribution in the inner region can be expected. A difference in the diffraction patterns of the data taken at 717 MeV and 71 MeV can be noticed in Fig. 7. The first diffraction minimum of the data taken at the energy of 71 MeV happens at around 1.5 fm^{-1}, while at the energy of 717 MeV it happens at around 2 fm^{-1}. As it is well known that nucleon–nucleon interactions are energy dependent, the shift of the diffraction patterns reflects a corresponding change in the nucleon–nucleon interactions at different incident energies of the presented datasets.

The following section presents a discussion of the obtained data using theoretical calculations. The theoretical model used is introduced in Sect. 4.1. In Sect. 4.2, a quantitative evaluation of the sensitivity is presented. This is done in order to understand what region of the nuclear density is probed the best by the present data and to decompose the effects of the inner (core) and peripheral (halo) parts of the density distribution to the differential cross section in a quantitative way. The response of the differential cross section to a corresponding change in the core and halo parts of the density is checked and the relative sensitivity to different parts of the density distribution is obtained. Such understanding is important in determining the direction of the analysis, and helps to relate the obtained data to the spatial structure of ^{6}He. To determine the density distribution a very detailed examination of the theoretical model used is required, which is beyond the scope of the present work and will be the main topic of future studies. In this work, we compare the obtained data to a set of theoretical calculations, assuming different density models of ^{6}He, to relate the data to its spatial structure. The comparison is carried out in Sect. 4.3. In Sect. 4.4, considering the obtained results, a set of recommendations is given to reliably determine the density distribution of ^{6}He for use in future analyses.

4. Discussion

4.1. *Relativistic impulse approximation model*

The investigations presented in the following subsections were carried out using relativistic impulse approximation (RIA) calculations. The RIA is known to provide an accurate description of the elastic scattering process at the incident energy of the present work. A detailed description of the model used is given in Refs. [18] and [33]. This subsection presents its brief description along with the calculation result to support the adequacy of the model.

The optical potential in RIA is determined by the Feynman amplitude for the nucleon–nucleon scattering and the relativistic nuclear density matrix of the target nucleus. For the nucleon–nucleon amplitudes, a revised version of IA2 parameterization is employed (S. J. Wallace, private communication). It is known to provide a successful description of the elastic scattering at the incident energy of the present work [33]. It uses a complete set of nucleon–nucleon amplitudes from a meson-exchange model and allows a parameter-free calculation of the optical potential. In the present work the parameter set for the incident energy of 200 MeV was used. The relativistic density matrix is defined by scalar, vector, and tensor components of the nuclear density. As the contribution of the tensor density to the differential cross section is known to be very small, it is omitted [34]. The scalar density is derived from the input vector density by multiplying it by a scalar-to-vector density factor obtained from relativistic mean field (RMF) calculations [35].

Since it has not been proven what level of accuracy can be expected from an RIA description of the proton elastic scattering from a light nucleus, to check this, we carried out an additional calculation. This was done to quantitatively confirm the adequacy of the model used. The RIA calculation was
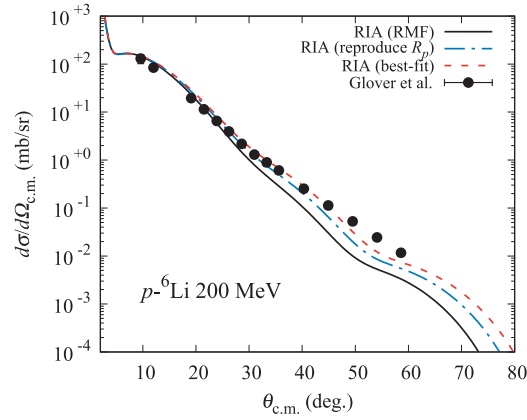
Fig. 8. Results of RIA calculations [18], using initial RMF (solid line), reproducing R_p (dash-dotted line) and best-fit (dashed line) densities of ^{6}Li. The experimental data are from Glover et al. [32] (solid circles). The error bars are comparable with the symbol size.

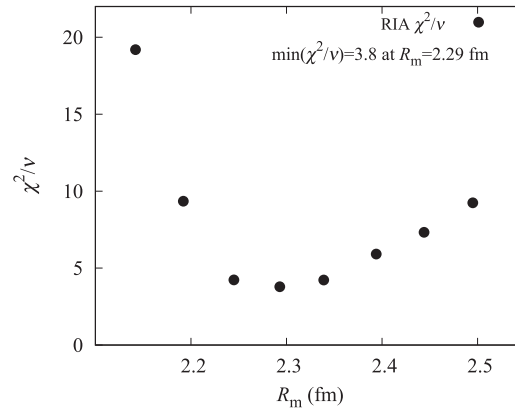**Fig. 9.** The distribution of the reduced χ^2 value (χ^2/ν, vertical axis) as a function of the matter radius (horizontal axis) of the RIA results of p–^{6}Li elastic scattering. The best-fit value of $R_\mathrm{m} = 2.29^{+0.07}_{-0.06}$ fm.

performed for another nucleus, ^{6}Li, which is an isobar of ^{6}He. The structure of ^{6}Li is considered to be similar to that of ^{6}He. Both are usually represented as consisting of an α-like core plus deuteron in the case of ^{6}Li or a two-neutron halo in the case of ^{6}He. A comparison of RIA differential cross sections of p–^{6}Li elastic scattering to the experimental data [32], assuming three input densities of ^{6}Li, is given in Fig. 8. The first differential cross section (solid line) assumes input density, which is a direct result of RMF calculations [35], and has a rather large matter radius of $R_\mathrm{m} = 2.52$ fm. The second one (dash-dotted line) assumes an RMF-based density, whose matter radius value was adjusted to reproduce the point-proton radius of $R_p = 2.39$ fm calculated from the results of charge radius measurements [1]. The last one (dashed line) assumes an RMF-based density, which gives the best fit to the data. The best-fit value of the matter radius is $R_\mathrm{m} = 2.29^{+0.07}_{-0.06}$ fm. The distribution of the reduced χ^2 values (χ^2/ν) as a function of the matter radius to p–^{6}Li data of Glover et al. [32] is given in Fig. 9. The errors, $^{+0.07}_{-0.06}$ fm, were determined as the region where the χ^2/ν value changes by $+1$ from its minimum value of 3.8. The difference between the best-fit result and point-proton radius of ^{6}Li (R_p) is almost the same as the experimental uncertainty (1.4σ).

Even though the matter radius of ^{6}Li was determined with good accuracy, to deduce the density distribution of ^{6}He, a much more detailed examination of the model used is necessary. The quality of

data reproduction has to be improved to further minimize the χ^2/ν value. The reason for the slightly large minimal value of $\chi^2/\nu = 3.8$ could be due to inaccuracies in the parameterization used for the nucleon–nucleon scattering amplitudes and the input density matrix. An effective interaction for $A = 6$ scattering has to be defined by fine-tuning of the input parameters for the nucleon–nucleon scattering amplitudes. The scalar-to-vector density ratio also has to be adjusted specifically for the case of $A = 6$ scattering, as it is known to change in very light nuclei in comparison to heavier ones [36]. Such analysis could be a topic of future studies, while the level of adequacy confirmed here is sufficient for the present work.

4.2.   Sensitivity of the elastic scattering at low and high momentum transfers to the density distribution

It is expected that elastic scattering at low momentum transfers ($q \leq 1$ fm^{-1}) is sensitive to the density at the surface of a nucleus, while the inner region is probed with higher momentum transfers. This expectation is based on the nature of the scattering amplitude as a product of the free proton–nucleon interaction amplitude and the nuclear form factor, which is a Fourier transform of the nuclear density distribution defined in a coordinate space to the momentum transfer space. It is the property of Fourier transform that suggests higher momentum transfers as a probe of the inner region of the density distribution. Elastic scattering at low momentum transfers ($q \leq 1$ fm^{-1}) was used to probe the outer part of ^{6}He density and to deduce its RMS matter radius [7]. In a recent study [17], it was confirmed that higher momentum transfer data are useful for deducing the inner part of the density distribution with higher precision. It is of interest to investigate the sensitivity of the elastic scattering data, taken in different momentum transfer regions, to different parts of the density distribution in a more quantitative way. Such knowledge allows the quantitative decomposition of the effects of the core and peripheral (halo) parts of the nuclear density distribution to the differential cross section. In this subsection, our aim is to evaluate the response of the elastic scattering cross sections to a change in density parameters, in order to understand how the density is probed by elastic scattering at different momentum transfers.

For the sensitivity study, a phenomenological Gaussian–Gaussian (GG) model of ^{6}He nucleon density distribution is used, which was defined in the previous work [7]. In the GG density distribution, the core and halo parts are described by the Gaussian functions

$$\rho_{c,h}(r) = A_{c,h} \left(\frac{3}{2\pi R_{c,h}^2} \right)^{3/2} \exp \left(-\frac{3r^2}{2R_{c,h}^2} \right), \tag{1}$$

where the radii of core (R_c) and halo (R_h) nucleon distributions are treated explicitly. R_c denotes the effective radius of the core, which is larger than the intrinsic radius of ^{4}He in free space (1.457 fm [37]) due to the internal motion of the core in ^{6}He. The parameters $A_c = 4$ and $A_h = 2$ denote the numbers of nucleons in the core (4 nucleons: 2 protons and 2 neutrons) and halo parts (2 neutrons), respectively. In the core part it is assumed that core protons and neutrons have the same density distributions: $\rho_c(r)/2$. The total matter density distribution ρ_m and the matter radius R_m are given by

$$\rho_m(r) = \rho_c(r) + \rho_h(r), \tag{2}$$

$$R_m = \left(\frac{A_c R_c^2 + A_h R_h^2}{A} \right)^{1/2}. \tag{3}$$

Table 2. GG nuclear density parameters used to test the sensitivity of the differential cross section. The first row gives the initial density parameters as deduced in Ref. [17], for comparison with the present data. In the following rows parameter values are given for the variation of RMS radii of core and halo nucleons relative to the initial density, to check the response of the observable. It is assumed that the radius of protons is equal to the core radius, $R_p = R_c$.

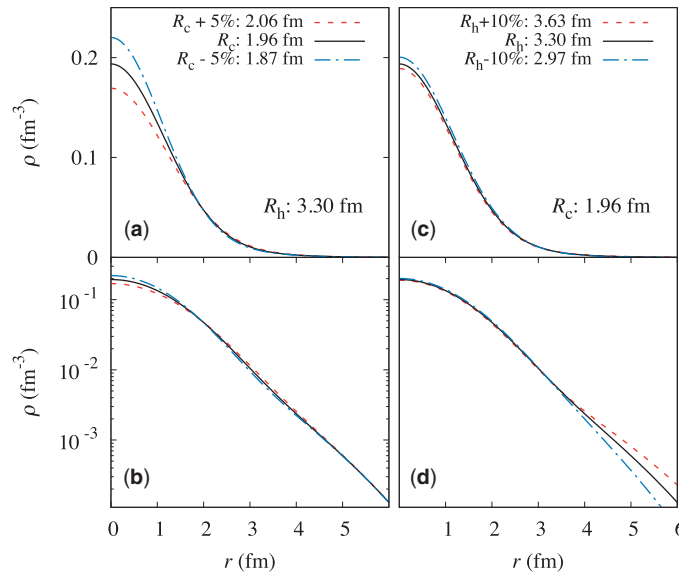| Density	R_c (fm)	R_h (fm)	R_n (fm)	R_m (fm)
Chung et al.	1.96	3.30	2.72	2.48
$R_c + 5\%$	2.06	3.30	2.75	2.54
$R_c - 5\%$	1.87	3.30	2.68	2.44
$R_h + 10\%$	1.96	3.63	2.92	2.64
$R_h - 10\%$	1.96	2.97	2.52	2.35

Fig. 10. Total matter density distributions using the GG density model, where RMS radii of core (panels (a) and (b)) and halo (panels (c) and (d)) nucleons were changed by $\pm 5\%$ and $\pm 10\%$ from the initial density deduced in Ref. [17].

Using this density parameterization, it is possible to separately check the response of the observable to a change in radii of the core and halo parts. For the initial parameters of the GG density distribution, the ones obtained in the previous study [17] are used. Based on the original density distribution, the core and halo radii are modified as summarized in Table 2. The corresponding density distributions are presented in Fig. 10.

Figures 11 and 12 show sets of differential cross sections, in low ($q \leq 1$ fm^{-1}) and high ($q = 1.7$–2.7 fm^{-1}) momentum transfer regions. The differential cross sections were obtained using different parameters of density from Table 2. The upper panels show observables, where the RMS radius of two valence neutrons was changed by $\pm 10\%$ (the halo part); the lower panels show the same but for a change in RMS radius of the core nucleons by $\pm 5\%$ (the core part). Our aim is to compare the sensitivity of the differential cross section to a change in the halo and core parts of the density in two momentum transfer regions. As can be seen from Fig. 11, at low momentum transfers, the difference in calculations due to a 10% change in R_h is a few times larger than that due to a 5% change in R_c; nearly equal sensitivity to a change in the radii of the halo and core parts can be observed ($\sim$1:1). Thus, the information from both halo and core parts couples in this momentum transfer region
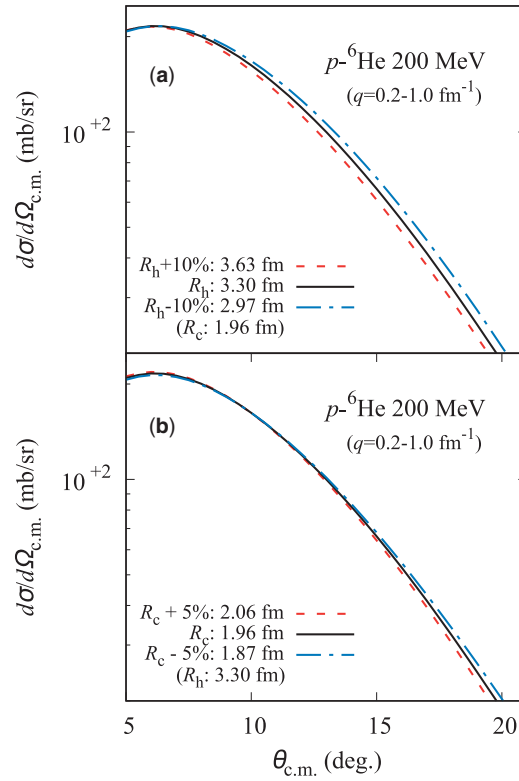
13/20

Fig. 11. Set of theoretical predictions based on RIA. The upper panel shows the sensitivity of the observable to a change in RMS radius of two valence neutrons. The lower one shows the sensitivity to a change in RMS radius of core nucleons. Both figures are given for the low momentum transfer region suitable for deduction of the outer part of the density.

($q < 1 \text{ fm}^{-1}$). This coupling might become a source of ambiguity in the determination of the density distribution parameters. On the other hand, as Fig. 12 demonstrates, when the momentum transfer is high, there is high sensitivity to a change in the core part, while the behavior of the tail part of the density is weakly probed. A 10% change in R_h induces a corresponding change of only ~8% in the absolute value of the cross section, while a twice as small 5% change in R_c induces a corresponding change of ~60% in the cross section value. In this momentum transfer region, the sensitivity to a change in the radius of the core part is larger than that to a corresponding change in the halo part by more than an order of magnitude (~15:1). The fact that data taken at high momentum transfers probe mostly the core part of the density makes it valuable to conclusively deduce the density of this region, without noticeable coupling to the halo part. At the same time, such data are not effective for determining the shape of the density in its tail, as it is probed very weakly. For this task, data taken at low momentum transfers are necessary. By fixing the density distribution of the core part using data taken at high momentum transfers, the parameters of the halo part can be deduced with higher accuracy as well, using data taken at low momentum transfers, as the coupling to the core becomes resolved. Thus, in order to determine the overall picture of the density distribution of ^{6}He, elastic scattering data taken in a wide range of momentum transfers are important.

4.3. Comparison to RIA theoretical predictions

In this subsection, the density distribution of ^{6}He is discussed by comparing the obtained data to a set of RIA predictions, which were made before the experiment [18]. In the previous subsection,
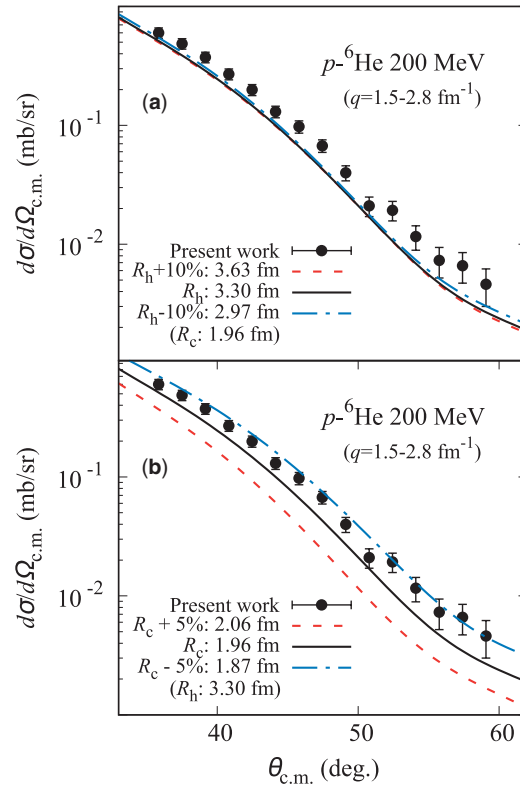
Fig. 12. Measured p–^{6}He differential cross sections along with a set of theoretical predictions based on RIA. The upper panel shows the sensitivity of the observable to a change in RMS radius of two valence neutrons. The lower one shows the sensitivity to a change in RMS radius of core nucleons. Both figures are given for the high momentum transfer region covered by the experimental data.

it was found that the present data serve as an exclusive probe of the inner region of ^{6}He density distribution and are thus valuable in deducing its structure. Considering this feature, the proton and neutron densities of ^{6}He around the center of the nucleus are related to the obtained data. The major goal of the comparison is to investigate the characteristics of the neutron density profile that are necessary to reproduce the data, given that the proton profile was fixed by using the charge radius information of ^{6}He. The importance of the charge radius information will also be demonstrated.

The RIA predictions have been made using modified RMF densities as described in Sect. 4.1 for the ^{6}Li case. Redistribution of the profiles was performed according to the following prescription:

$$A - Z, Z = 4\pi \int \rho_{n,p}(r) r^2 dr = 4\pi a^{-3} \int \tilde{\rho}_{n,p}(x) x^2 dx, \qquad (4)$$

where $r = x/a$ and A, Z are the nuclear mass number and the atomic number, respectively. The density distribution denoted by $\rho_{n,p}(r)$ was obtained from the RMF calculation. The profile $\tilde{\rho}_{n,p}(x)$ describes the expanded distribution for $a > 1$ and a contracted one for $a < 1$ with respect to the RMF density $\rho_{n,p}(r)$. During redistribution, normalization by the nucleon number was preserved. The three panels in Fig. 13 show modified distributions of the proton, neutron, and total matter density profiles given in Ref. [18]. Table 3 gives a summary of the corresponding RMS radii. In the table, "tma" in the first column corresponds to the result of the RMF calculation. Figure 13(a) represents tmav1, a modified RMF density, where the proton distribution was compressed slightly to reproduce the
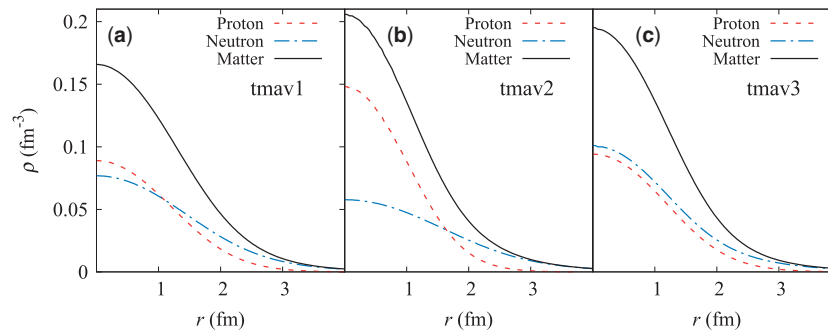
15/20

Fig. 13. Proton and neutron density distributions of ^{6}He based on RMF calculations [18]. Panels (a), (b), and (c) present distributions of three different densities: tmav1, tmav2, and tmav3, respectively.

Table 3. RMS radii of the proton (R_p), neutron (R_n), and total matter (R_m) distributions of the RMF-based densities of ^{6}He [18].

Model	R_p (fm)	R_n (fm)	R_m (fm)
tma	2.044	3.050	2.75
tmav1	1.937	3.050	2.73
tmav2	1.635	3.352	2.89
tmav3	1.936	3.214	2.85
$R_p^{\rm ch}$	1.938(23)		

known point-proton radius of ^{6}He, which RMF overestimates. The point-proton radius of ^{6}He was calculated from the measured charge radius [37] and is given by $R_p^{\rm ch}$ in Table 2. The neutron density of tmav1 is an unmodified result of the RMF calculation. The model of tmav2 (Fig. 13(b)) has a compressed proton and an expanded neutron distribution. The third modified distribution, tmav3 (Fig. 13(c)), is consistent with the model of ^{6}He as an α-like core + two-neutron halo nucleus. In this density distribution $R_p^{\rm ch}$ is also reproduced by the proton profile. The neutron profile has almost the same shape as the proton one around the center of ^{6}He. Consequently, the two protons and two neutrons in the inner region have similar radii, forming an α-like core, and the halo is formed by two other neutrons. The tmav3 density can be considered as the most realistic model of the ^{6}He nucleus.

The three RMF-based density distributions that were introduced above show different behaviors for the neutron and proton density profiles in the inner region of the nucleus, as Fig. 13 demonstrates. Figure 14 shows a set of differential cross sections assuming the three RMF-based densities along with the present experimental result. The data are reproduced the best by the calculation assuming tmav3 density with a reduced χ^2 value of $\chi^2/\nu = 0.3$, with tmav2 in slight disagreement, having $\chi^2/\nu = 2.2$, while the one assuming tmav1 density clearly disagrees with the data with $\chi^2/\nu = 6.3$. Interpretation of the comparison is given below.

The major purpose of the discussion in this subsection is to investigate the characteristics of the neutron density profile, given that the proton profile was fixed by using ^{6}He charge radius information. For this, two densities are used: tmav1 and tmav3, whose proton density profiles are same and were adjusted to reproduce the point-proton radius, $R_p^{\rm ch}$, while their neutron profiles are different. The neutron profile in tmav1 is more spread out around the center of ^{6}He in comparison to the proton profile, thus testing for the assumption that the proton and neutron distributions behave independently.

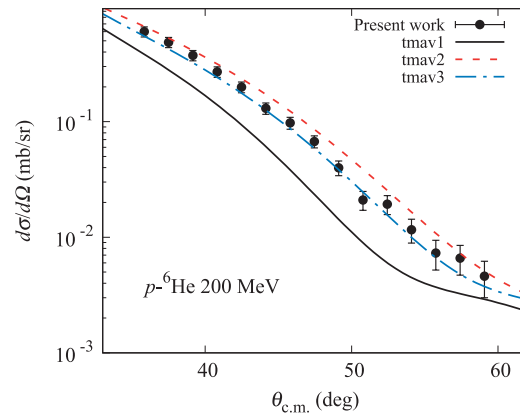**Fig. 14.** Results of RIA calculations [18], assuming three RMF-based density distributions of ^{6}He (displayed in Fig. 13) along with the present experimental result of the differential cross sections.

On the other hand, in tmav3, the neutron density profile behaves very similarly to the proton one, testing the assumption that ^{6}He is a nucleus with a rigid α-like core + two-neutron halo. The results of the calculations assuming tmav1 and tmav3 densities can be easily distinguished using the present experimental result. The effect of a more expanded neutron distribution in tmav1 significantly affects the observable and this feature is not supported by the data. Given that the proton density profile reproduces the realistic point-proton radius of ^{6}He, to reproduce the data, the neutron distribution around the center of ^{6}He should have almost the same shape as the proton one. Here, it was shown that the data are reproduced using the density distribution with the radius of its proton profile tuned to agree with the charge radius information and with the radius of the core part of its neutron profile similar to that of the proton. From this comparison it can be concluded that the density model of ^{6}He is consistent with the assumption that it is a nucleus with a rigid α-like core whose proton and neutron density profiles are almost the same and reproduce the point-proton radius of ^{6}He obtained from the charge radius measurements. A more detailed analysis to determine a model-independent density distribution will be done in future by using a carefully examined reaction model, as described in the following subsection.

An additional purpose of the comparison to theoretical calculations is to demonstrate the importance of the charge radius information along with proton elastic scattering data in order to be able to distinguish proton and neutron densities. For this, the data are compared to the tmav2 and tmav3 densities. The tmav2 density distribution has a very different proton and neutron profiles around the center of ^{6}He, preserving the total matter radius as that of tmav3. This density tests for the possibility of distinguishing the contributions of the proton and neutron densities to the observable without relying on the presence of the charge radius information. The differential cross section assuming tmav2 density distribution is close to the one assuming tmav3 and cannot be easily distinguished by the data. The compressed proton density profile of tmav2 is compensated by its extended neutron density distribution. This feature gives the profile of the total matter density distribution, which is similar to that of tmav3; this is reflected in the behavior of the corresponding differential cross sections. This fact emphasizes the importance of information on the charge radius or other additional information of such kind along with the proton elastic scattering data taken at a single incident energy. Some methods for the decomposition of the proton and neutron distributions are described in the following subsection.

4.4.   Prospects for the study of density distributions via proton elastic scattering

Proton elastic scattering is a well established method for deducing the radial shapes of nuclear density distributions of stable and unstable nuclei. As has been shown in the present work, the sensitivity of elastic scattering data to details of the density distribution varies with the value of momentum transfer. The surface region can be probed at $q < 1$ fm^{-1}, while higher values of momentum transfer are needed for the inner region. From the experience of the present work, the differential cross section measured up to the second diffractive minimum, which occurs at $q \approx 2.5$–3 fm^{-1}, is sufficient to constrain the parameters of the density distribution with high precision. The choice of incident energy of 200–300 MeV can be justified by the condition that the mean free path of the probe particle should be maximized. In this case, the nucleus appears to be the most transparent to the probe particle, thus making it easier to obtain information on its inner part. In order to obtain an overall picture of the density distribution of ^{6}He, proton elastic scattering data are needed in a wide range of momentum transfers, starting from $q \approx 0$ fm^{-1}, and covering up to 2.5–3 fm^{-1} at 200–300 MeV.

As was demonstrated in the previous subsection, it is difficult to distinguish the contributions of the proton and neutron densities using only the proton elastic scattering data taken at a single incident energy. To determine the proton and neutron densities separately additional information is required. A well known source of such information is the results of charge density measurements by means of electron scattering, which are available for a wide range of stable nuclei [1]. Promising results have been achieved to develop a method of electron scattering that is applicable to unstable nuclei [13]. Another possibility is to use proton elastic scattering at two significantly different incident energies to separately determine the proton and neutron densities of unstable nuclei [2]. The method has already been confirmed to work for a stable nucleus, ^{90}Zr. It relies on the difference of nucleon–nucleon cross sections at different incident energies, allowing the separation of the proton and neutron densities. By complementing the proton elastic scattering taken at a single incident energy with information from one of the proposed methods one can separately determine the nucleon density distributions.

In this work, using RIA calculations, it has been shown that elastic scattering data at high momentum transfers, covered by the present work, are sensitive to the core part of ^{6}He density. The fact that the RIA result for p–^{6}Li elastic scattering shown in Fig. 8 reproduces the experimental data, having a reduced χ^2 value of 3.8, implies that RIA using IA2 parameterization (S. J. Wallace, private communication) can be a good candidate for a model to derive the ^{6}He density distribution from the present data. However, in order to reliably deduce the density distribution of ^{6}He, one needs careful examination of all aspects of the theoretical model employed, to evaluate all possible sources of uncertainties that might result from the assumed density model, the chosen parameterization of nucleon–nucleon scattering amplitudes, and the definition of the input density matrix. The possible need for adjustment of the nucleon–nucleon scattering amplitudes used should be considered to obtain the best reproduction of the experimental data of a nucleus whose density distribution has been reliably determined. Fine-tuning of the scalar-to-vector density ratio should also be considered as it is known to change in light nuclei, compared to that in heavier elements [36]. An analysis using a model-independent definition of the density, such as the sum-of-Gaussians [38], is preferred over the use of phenomenological density models. A more detailed analysis considering the details mentioned is left for future work.

Apart from the differential cross section, the vector analyzing power data can serve as an additional constraint for the interaction and nuclear density inputs of the reaction model chosen to analyze the

data. Thus, the availability of the analyzing power data also helps to increase the reliability of the deduced density distribution.

5. Summary

In this work, the differential cross sections of p–^{6}He elastic scattering at 200 A MeV were measured in a high momentum transfer region of 1.7–2.7 fm^{-1}. Using relativistic impulse approximation (RIA) calculations, the sensitivity of the differential cross section to ^{6}He density was evaluated. It was found that in the momentum transfer region covered by the present work, the sensitivity to a change in the core part of the density distribution is larger than that to a corresponding change in the halo part by more than an order of magnitude ($\sim$15:1), while at lower momentum transfers of less than 1 fm^{-1}, the sensitivity to a change in the core and halo parts is similar (1:1). Therefore, the newly obtained data serve as an exclusive probe for the α core distribution in the ^{6}He nucleus. Also, it was pointed out that to obtain an overall picture of the density distribution, proton elastic scattering data taken at a single incident energy of 200–300 MeV and in a wide momentum transfer region are important. The obtained data were compared to a set of RIA calculations assuming density models based on the result of relativistic mean field (RMF) calculations. It was shown that the data are well reproduced by the calculation assuming almost the same profiles of proton and neutron densities around the center of ^{6}He, and a proton profile reproducing the known point-proton radius of 1.94 fm. This finding is consistent with the assumption that the ^{6}He nucleus consists of a rigid α-like core with a two-neutron halo. To reliably deduce the density distribution, a more detailed analysis has to be carried out, considering all possible sources of uncertainties that might result from the nucleon–nucleon scattering amplitudes used, the definition of the density matrix, and the density model. Such analysis will be a topic of future work. Vector analyzing power data will also be important for the validation of the interaction used for the deduction of the density distribution.

References

[1] H. De Vries, C. W. De Jager, and C. De Vries, At. Data Nucl. Data Tables **36**, 495 (1987).
[2] H. Sakaguchi and J. Zenihiro, Prog. Part. Nucl. Phys. **97**, 1 (2017).
[3] P. Egelhof et al., Eur. Phys. J. A **15**, 27 (2002).
[4] A. A. Korsheninnikov et al., Nucl. Phys. A **617**, 45 (1997).
[5] A. Lagoyannis et al., Phys. Lett. B **518**, 27 (2001).
[6] S. V. Stepantsov et al., Phys. Lett. B **542**, 35 (2002).
[7] G. D. Alkhazov et al., Nucl. Phys. A **712**, 269 (2002).
[8] A. N. Antonov, M. K. Gaidarov, D. N. Kadrev, P. E. Hodgson, and E. Moya de Guerra, Int. J. Mod. Phys. E **13**, 759 (2004).
[9] O. A. Kiselev et al., Eur. Phys. J. A **25** (Suppl. 1), 215 (2005).
[10] T. Uesaka et al., Phys. Rev. C **82**, 021602(R) (2010).
[11] S. Sakaguchi et al., Phys. Rev. C **84**, 024604 (2011).

[12] Y. Matsuda et al., Phys. Rev. C **87**, 034614 (2013).
[13] T. Suda and H. Simon, Prog. Part. Nucl. Phys. **96**, 1 (2017).
[14] I. Tanihata, H. Hamagaki, O. Hashimoto, Y. Shida, N. Yoshikawa, K. Sugimoto, O. Yamakawa, T. Kobayashi, and N. Takahashi, Phys. Rev. Lett. **55**, 2676 (1985).
[15] L.-B. Wang et al., Phys. Rev. Lett. **93**, 142501 (2004).
[16] L. V. Chulkov, C. A. Bertulani, and A. A. Korsheninnikov, Nucl. Phys. A **587**, 291 (1995).
[17] L. X. Chung, O. A. Kiselev, D. T. Khoa, and P. Egelhof, Phys. Rev. C **92**, 034608 (2015).
[18] K. Kaki, Phys. Rev. C **89**, 014620 (2014).
[19] M. Toyokawa, K. Minomo, and M. Yahiro, Phys. Rev. C **88**, 054602 (2013) [arXiv:1304.7884 [nucl-th]] [Search INSPIRE].
[20] S. P. Weppner and Ch. Elster, Phys. Rev. C **85**, 044617 (2012) [arXiv:1107.1816 [nucl-th] [Search INSPIRE].
[21] Y. Yano, Nucl. Instrum. Meth. Phys. Res. B **261**, 1009 (2007).
[22] A. Yoshida, T. Suda, T. Ohtsuki, H. Yuki, and T. Kubo, Nucl. Instrum. Meth. Phys. Res. A **590**, 204 (2008).
[23] T. Kubo, Nucl. Instrum. Meth. Phys. Res. B **204**, 97 (2003).
[24] H. Sato et al., IEEE Trans. Appl. Supercond. **23**, 4500308 (2013).
[25] T. Kobayashi et al., Nucl. Instrum. Meth. Phys. Res. B **317**, 294 (2013).
[26] T. Wakui, M. Hatano, H. Sakai, T. Uesaka, and A. Tamii, Nucl. Instrum. Meth. Phys. Res. A **550**, 521 (2005).
[27] J. Zenihiro et al., Proc. French-Japanese Symp. Nuclear Structure Problems: Wako, Japan, January 5–8, 2011, p. 214 (2012).
[28] P. U. Renberg, D. F. Measday, M. Pepin, P. Schwaller, B. Favier, and C. Richard-Serre, Nucl. Phys. A **183**, 81 (1972).
[29] G. A. Moss et al., Phys. Rev. C **21**, 1932 (1980).
[30] S. R. Neumaier et al., Nucl. Phys. A **712**, 247 (2002).
[31] O. A. Kiselev et al., Nucl. Instrum. Meth. Phys. Res. A **641**, 72 (2011).
[32] C. W. Glover et al., Phys. Rev. C **41**, 2487 (1990).
[33] J. A. Tjon and S. J. Wallace, Phys. Rev. C **36**, 1085 (1987).
[34] L. G. Arnold and B. C. Clark, Phys. Lett. B **84**, 46 (1979).
[35] Y. Sugahara and H. Toki, Nucl. Phys. A **579**, 557 (1994).
[36] M. Yoshimura et al., Phys. Rev. C **63**, 034618 (2001).
[37] P. Mueller et al., Phys. Rev. Lett. **99**, 252501 (2007).
[38] I. Sick, Phys. Lett. B **44**, 62 (1973).